Monthly Notices
of the
ROYAL ASTRONOMICAL SOCIETY

MNRAS **460,** 2675–2686 (2016)
Advance Access publication 2016 May 10

doi:10.1093/mnras/stw1097

Giant Metrewave Radio Telescope observations of neutral atomic hydrogen gas in the COSMOS field at $z \sim 0.37$

Jonghwan Rhee,[1,2,3]★† Philip Lah,[1,4] Jayaram N. Chengalur,[4] Frank H. Briggs[1,3] and Matthew Colless[1,3]

[1]*Research School of Astronomy and Astrophysics, Australian National University, Canberra, ACT 2611, Australia*
[2]*International Centre for Radio Astronomy Research (ICRAR), University of Western Australia, Crawley, WA 6009, Australia*
[3]*ARC Centre of Excellence for All-sky Astrophysics (CAASTRO)*
[4]*National Centre for Radio Astrophysics, Tata Institute for Fundamental Research, Pune 411 007, India*

Accepted 2016 May 6. Received 2016 May 5; in original form 2015 October 8

ABSTRACT

We present the results of H I spectral stacking analysis of Giant Metrewave Radio Telescope (GMRT) observations targeting the Cosmological Evolution Survey (COSMOS) field. The GMRT data cube contains 474 field galaxies with redshifts known from the zCOSMOS-bright 10 k catalogue. Spectra for the galaxies are co-added and the stacked spectrum allows us to make a $\sim 3\sigma$ measurement of the average H I mass. Using this average H I mass, along with the integral optical *B*-band luminosity of the galaxies and the luminosity density of the COSMOS field, a volume normalization is applied to obtain the cosmic H I mass density ($\Omega_{\rm H\,I}$). We find a cosmic H I mass density of $\Omega_{\rm H\,I} = (0.42 \pm 0.16) \times 10^{-3}$ at $z \sim 0.37$, which is the highest redshift measurement of $\Omega_{\rm H\,I}$ ever made using H I spectral stacking. The value we obtained for $\Omega_{\rm H\,I}$ at $z \sim 0.37$ is consistent with that measured from large blind 21-cm surveys at $z = 0$, as well as measurements from other H I stacking experiments at lower redshifts. Our measurement, in conjunction with earlier measurements, indicates that there has been no significant evolution of H I gas abundance over the last 4 Gyr. A weighted mean of $\Omega_{\rm H\,I}$ from all 21-cm measurements at redshifts $z \lesssim 0.4$ gives $\Omega_{\rm H\,I} = (0.35 \pm 0.01) \times 10^{-3}$. The $\Omega_{\rm H\,I}$ measured (from H I 21-cm emission measurements) at $z \lesssim 0.4$ is, however, approximately half that measured from damped Lyman-α absorption (DLA) systems at $z \gtrsim 2$. Deeper surveys with existing and upcoming instruments will be critical to understand the evolution of $\Omega_{\rm H\,I}$ in the redshift range intermediate between $z \sim 0.4$ and the range probed by DLA observations.

Key words: galaxies: evolution – galaxies: ISM – radio lines: galaxies.

1 INTRODUCTION

Our knowledge of the evolution of galaxies has been acquired almost exclusively by large-scale surveys using ground- and space-based telescopes at optical and adjacent wavelengths (e.g. York et al. 2000; Colless et al. 2001; Martin et al. 2005; Skrutskie et al. 2006). The information obtained from these surveys is mainly valuable for tracing the evolution of the stellar content of galaxies. In contrast, little is known about the evolution of the (cold) gaseous component in galaxies. In particular, our knowledge of the neutral atomic hydrogen gas (H I) content (i.e. the raw material for star formation) of individual galaxies is essentially limited to the very low redshift Universe (Meyer et al. 2004; Haynes et al. 2011).

Understanding the evolution of the atomic gas content of galaxies remains one of the key challenges in the study of galaxy evolution. The sensitivity of the current generation of radio telescopes is insufficient to detect H I from individual galaxies at cosmologically significant redshifts in reasonable integration times. Indeed, the detection of H I from individual galaxies at high redshifts was one of the original motivations, and remains one of the key science drivers, for the proposed Square Kilometre Array (SKA: e.g. Blyth et al. 2015; Santos et al. 2015; Staveley-Smith & Oosterloo 2015). It is also one of the key programmes for several of the upcoming SKA pathfinder telescopes, for instance the Widefield ASKAP *L*-band Legacy All-sky Blind surveY (WALLABY: Koribalski & Staveley-Smith 2009), the Deep Investigation of Neutral Gas Origins (DINGO: Meyer 2009) and Looking At the Distant Universe with the MeerKAT Array (LADUMA: Holwerda, Blyth & Baker 2012). In combination with data at other wavelengths, this knowledge of H I gas obtained from the SKA and its pathfinders will

★E-mail: jonghwan.rhee@icrar.org
† Now at ICRAR.

allow us to understand fully the complex processes that govern galaxy evolution (Meyer et al. 2015).

Although it is challenging to detect H I in individual galaxies at $z \gtrsim 0.2$ with the current generation of radio telescopes, it is possible to make measurements of the average H I content of a sample of galaxies. The volume of space probed in a single pointing and correlator setting typically contains many hundreds of galaxies. If the positions and redshifts of all of these galaxies are known, one can stack their spectra to determine their average H I content (Chengalur, Braun & Wieringa 2001; Zwaan, van Dokkum & Verheijen 2001). This spectral stacking technique has been applied to interferometers such as the Giant Metrewave Radio Telescope (GMRT) and the Westerbork Radio Telescope (WSRT), as well as single dishes such as the Parkes, to measure the H I content of galaxies at redshifts $z \lesssim 0.4$, resulting in determination of the evolution of the gas content in galaxies (i.e. $\Omega_{\rm H\,I}$) out to redshifts $z \sim 0.2$ (Lah et al. 2007, 2009; Delhaize et al. 2013; Rhee et al. 2013).

Here, we apply the technique to GMRT observations of the COSMOS field to determine $\Omega_{\rm H\,I}$ at a redshift of $z \sim 0.37$. The GMRT observation of the COSMOS field plays an important role as a precursor of future H I deep surveys using SKA pathfinders. To check the viability of the surveys and develop suitable observing modes and strategies, a smaller-scale H I survey, as presented here, is a good testbed. Both expected and unexpected issues relevant to wide and deep H I surveys can be explored through such a pilot study. The redshift studied ($z \sim 0.37$) allows us to understand how the H I gas in galaxies evolves out to $z \sim 0.4$ and perhaps beyond.

This article is structured as follows. In Section 2 we detail the optical data of the COSMOS field. Section 3 describes the GMRT observations, data quality and data reduction procedures. We explain the stacking analysis used to measure the average H I gas mass at $z \sim 0.37$ in Section 4. The main results are presented in Section 5. In Section 6, we discuss the implications of our observations for the cosmic evolution of $\Omega_{\rm H\,I}$. We present a summary and conclusions in Section 7. Throughout the article, we adopt the concordance cosmological parameters: $\Omega_\Lambda = 0.7$, $\Omega_{\rm M} = 0.3$ and $H_0 = 70$ km s^{-1} Mpc^{-1}.

2 DATA

2.1 Target field selection

Our radio observations are centred on the COSMOS field. This field has a wealth of multi-wavelength data ranging from X-ray to radio (Scoville et al. 2007). Spectroscopic redshifts are also available for a very large number of galaxies in the COSMOS field (zCOSMOS: Lilly et al. 2007). This makes it an excellent target for H I studies. Indeed, it has also been selected as the target for a very deep Karl G. Jansky Very Large Array (JVLA) H I survey (the COSMOS H I Large Extragalactic Survey (CHILES): Fernández et al. 2013).

2.2 Photometric data

Optical positions and redshifts are crucial inputs required for H I stacking analysis. Multi-band photometric data are also very important, because they allow one to determine the cosmic H I density as well as the dependence of H I gas content on other galaxy properties, such as the morphological or spectral type, etc. Photometry of the galaxies in the COSMOS field is available over a very large range of wavelengths: X-ray with *XMM–Newton* (Hasinger et al. 2007), UV with the *Galaxy Evolution Explorer* (*GALEX*: Zamojski et al. 2007), optical/NIR with the Canada–France–Hawaii Telescope (CFHT), Cerro Tololo Inter-American Observatory (CTIO), Kitt Peak National Observatory (KPNO), Subaru (Taniguchi et al. 2007) and *Hubble Space Telescope* (*HST*: Koekemoer et al. 2007), mid-infrared with the *Spitzer* space telescope (Sanders et al. 2007), mm/submillimetre with the Caltech Submillimeter Observatory (CSO) and Institut de Radioastronomie Millimétrique (IRAM) telescope (Bertoldi et al. 2007) and radio continuum with the Very Large Array (VLA: Schinnerer et al. 2004, 2007).

Table 1. Photometric band filters and their zero-point offsets in the COSMOS photometry catalogue taken from Ilbert et al. (2009). All magnitudes of our sample in these photometric bands were used as inputs for the SED fitting procedure with LE PHARE.

Filter	Telescope	$\lambda_{\rm eff}$ (Å)	FWHM (Å)	Offset
FUV	*GALEX*	1551.3	230.8	0.314
NUV	*GALEX*	2306.5	789.1	−0.022
u^*	CFHT	3911.0	538.0	0.054
B_J	Subaru	4439.6	806.7	−0.242
V_J	Subaru	5448.9	934.8	−0.094
g^+	Subaru	4728.3	1162.9	0.024
r^+	Subaru	6231.8	1348.8	0.003
i^+	Subaru	7629.1	1489.4	0.019
i^*	CFHT	7628.9	1460.0	−0.007
z^+	Subaru	9021.6	955.3	−0.037
J	UKIRT	12444.1	1558.0	0.124
K_s	KPNO/CTIO	21434.8	3115.0	0.022
K	CFHT	21480.2	3250.0	−0.051
*IA*427	Subaru	4256.3	206.5	0.037
*IA*464	Subaru	4633.3	218.0	0.013
*IA*484	Subaru	4845.9	228.5	0.000
*IA*505	Subaru	5060.7	230.5	−0.002
*IA*527	Subaru	5258.9	242.0	0.026
*IA*574	Subaru	5762.1	271.5	0.078
*IA*624	Subaru	6230.0	300.5	0.002
*IA*679	Subaru	6778.8	336.0	−0.181
*IA*709	Subaru	7070.7	315.5	−0.024
*IA*738	Subaru	7358.7	323.5	0.017
*IA*767	Subaru	7681.2	364.0	0.041
*IA*827	Subaru	8240.9	343.5	−0.019
*NB*711	Subaru	7119.6	72.5	0.014
*NB*816	Subaru	8149.0	119.5	0.068

We cross-matched the zCOSMOS redshift catalogue with the publicly released photometric catalogue of the COSMOS field from the NASA/IPAC Infrared Science Archive (IRSA) website.[1] This provides observed magnitudes in 27 photometric bands covered by CFHT, Subaru, KPNO/CTIO and *GALEX*. This catalogue is an update on the previous optical/NIR catalogue by Capak et al. (2007). The updated photometric catalogue was compiled using the same point-spread function (PSF) from u^* to the K band. The photometry was derived over the same aperture of 3-arcsec diameter centred on the position of i^+ and i^* bands. For other bands such as the far-ultraviolet (FUV) and near-ultraviolet (NUV), wide-aperture total fluxes were measured first and then converted to 3-arcsec aperture flux. This consistency in measuring photometry allows us to determine accurate colours, leading to small uncertainties in the measurement of the spectral energy distribution (SED) fitting for k-correction, galaxy classification and measurement of the stellar mass. A more detailed description of the photometric catalogue can be found in Capak et al. (2007) and Ilbert et al. (2009).

Table 1 lists the photometric bands that we used in our analysis. We corrected all magnitudes for the zero-point offset listed in

[1] http://irsa.ipac.caltech.edu/data/COSMOS/

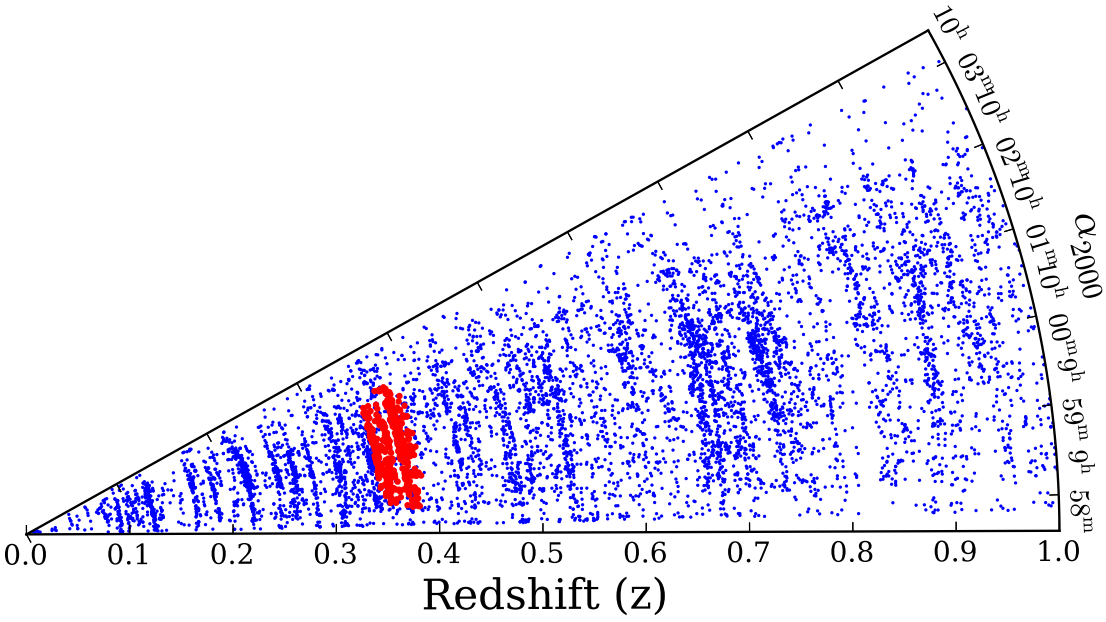

Figure 1. Redshift cone diagram of zCOSMOS 10 k-bright sample to $z \sim 1$. Red and big points denote the 506 galaxies covered by the GMRT beam and frequency at $z \sim 0.37$.

Table 1 following Ilbert et al. (2009) and then applied the corrections for Galactic dust extinction using the dust map of Schlegel, Finkbeiner & Davis (1998). *k*-corrections were also applied for all magnitudes using values obtained through a χ^2 template-fitting procedure.

2.3 Spectroscopic data

Our spectroscopic data are taken from the zCOSMOS (Lilly et al. 2007) survey. The zCOSMOS survey (Lilly et al. 2007) is a large optical redshift survey undertaken in the COSMOS field using the VIsible Multi-Object Spectrograph (VIMOS) mounted on the Very Large Telescope (VLT) at the European Southern Observatory (ESO), Chile. The main goal of the survey was to trace the large-scale structure of the Universe up to $z \sim 1$ and to characterize galaxy groups and clusters. The zCOSMOS survey consists of two distinct parts, called zCOSMOS-bright and zCOSMOS-deep. zCOSMOS-bright is a magnitude-limited survey ($I_{AB} < 22.5$ measured in the *I* band of the *HST* Advanced Camera for Surveys (ACS)), targeting ∼20 000 galaxies in the redshift range $0.1 < z < 1.2$ (see Fig. 1). This survey was undertaken on the entire 1.7 deg^2 COSMOS field. zCOSMOS-deep surveys ∼10 000 galaxies, colour-selected to be in the range $1.4 < z < 3.0$, in the central 1 deg^2 of the COSMOS field.

In this article, the spectroscopic data used come from the zCOSMOS-bright catalogue, which has spectra for 10 644 objects, the so-called 10k-bright sample. These contain a statistically complete subset of 10 109 objects. Spectra obtained from the zCOSMOS-bright survey cover a wavelength range of approximately 5550–9450 Å, yielding a spectral resolution of $R \sim 600$ sampled at ∼2.5 Å pixel^{-1}. The velocity uncertainty of the zCOSMOS-bright redshifts is ∼110 km s^{-1}. For more details about data and data reduction, refer to Lilly et al. (2007, 2009). The zCOSMOS 10k-bright catalogue provides redshifts along with confidence classes indicating the reliability of its redshift measurements. The confidence classes (see table 1 of Lilly et al. 2009) vary from class 0 (no redshift obtained) to class 4 (most secure redshift), with an additional class 9 for one-line redshifts where the line is believed to be either [O II] or H α. For the analysis in this article, we restrict the sample to galaxies with the most secure redshift, i.e. those in class 3 or 4. This selection produces a sample of 506 redshifts with reliable redshifts that lie within the GMRT data cube (∼1 deg^2 at the observed frequency, 1040 MHz) and the redshift range of $0.35 < z < 0.39$ (see also Fig. 5, later).

2.4 Galaxy classification

We used two different methods to classify our sample galaxies: one based on galaxy morphology and the other on spectrophotometry. The COSMOS field has the *HST* ACS imaging data (Koekemoer et al. 2007) with sufficient depth and resolution to perform morphological analysis. The COSMOS archival data base provides a morphological class catalogue, which is based on applying an automatic and objective morphological classification technique to high-quality *HST* images (Cassata et al. 2007; Tasca et al. 2009). The morphological classification divides the galaxies into three morphological classes: early-types including ellipticals and lenticulars, spirals and irregulars.

The spectrophotometric classification is based on matching the rest-frame magnitudes and colours to a set of templates. Here, LE PHARE[2] (Arnouts et al. 1999; Ilbert et al. 2006), a χ^2 template-fitting code, using 20 photometric magnitudes from the COSMOS photometry catalogue, was applied in combination with spectroscopic redshifts from the zCOSMOS catalogue for each galaxy in the sample. This spectrophotometric classification divides our sample galaxies into four types: early-type E/S0 (Type 1), early spirals Sa/Sb (Type 2), late spirals Sc/Sd (Type 3) and irregular and starburst galaxies (Type 4).

Following Ilbert et al. (2009) and Williams et al. (2009), we used $u^* - V$ versus $V - J$ and $NUV - r_+$ versus $r_+ - J$ colour–colour diagrams to compare these two classification schemes. In Fig. 2,

[2] http://www.cfht.hawaii.edu/∼arnouts/lephare.html

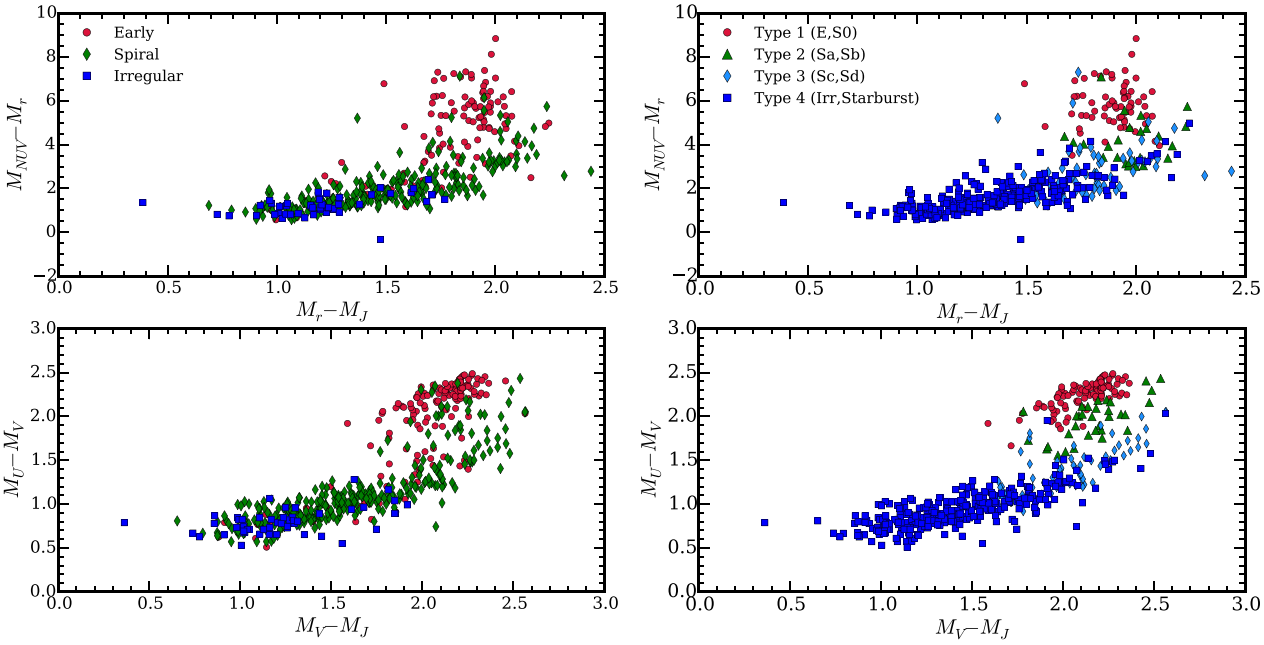

Figure 2. Colour–colour diagrams of subsamples classified by morphological (left panels) and spectrophotometric (right panels) approaches. The upper panels are $NUV - r_+$ and $r_+ - J$ colour–colour diagrams and the lower panels are $u^* - V$ and $V - J$ colour–colour diagrams. In each panel on the left, morphological subclasses of early-types, spirals and irregulars are shown by red circles, green diamonds and blue squares, respectively. Four subsamples of the spectrophotometric approach from Type 1 to Type 4 are denoted in the right panels by red circles, green triangles, blue diamonds and squares.

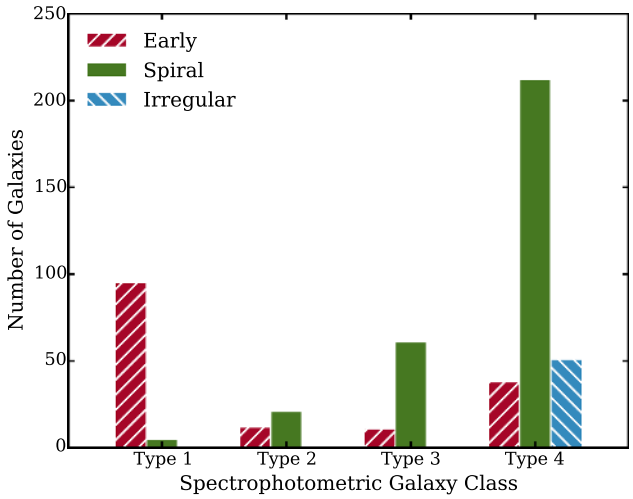

Figure 3. The spectrophotometric classes of galaxies classified morphologically. Red (/), green, and blue (\) bars denote morphological classes: early, spiral and irregular, respectively.

the left-hand panels plot the morphological classes of the galaxies, while the right-hand panels show the spectrophotometric classes. As can be seen, the morphologically classified early-types and spirals are not sharply separated in these diagrams. In particular, there are galaxies that are morphologically classified as early type but are blue in colour. Fig. 2 shows that spectrophotometry provides a much cleaner separation. Fig. 3 summarizes the leakage of the morphological classes between the spectrophotometric classes.

Visual inspection of the *HST* images of blue early-types shows that some of them have an obvious spiral or ring feature, as seen in the upper row of Fig. 4. This indicates that the uncertainty in the morphological classification can affect the H I stacking analysis for different galaxy types, as detailed below. Although the

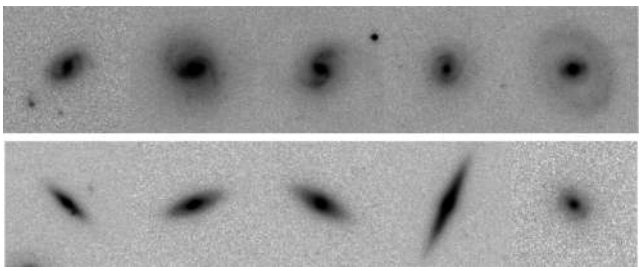

Figure 4. *HST* cutout images of blue early-type (upper row) and red spiral (lower row) examples. The size of each thumbnail image is 6×6 arcsec^2. The images were obtained using the G10/COSMOS image-cutout tool.

spectrophotometry clearly separates the early-types, there exist Type 1 galaxies having spiral morphology (called 'red spirals'). These galaxies look to be highly inclined or edge-on spirals in their *HST* images (see the lower row of Fig. 4). Their high inclination can cause more internal reddening by dust, resulting in a redder colour and a mismatched template. These galaxies have a negligible effect on the H I stacking analysis, because the fraction of such galaxies is below 5 per cent. We have adopted the spectrophotometric classification in our further analysis.

3 GMRT RADIO DATA

3.1 Observations

The zCOSMOS field was observed for a total of 134 h using the GMRT. The observations were conducted over 20 d spread over the years 2008 and 2009. The total observation time includes 115 h of on-source time, with the remaining time spent on calibrator scans. The central frequency of the GMRT observations was 1040 MHz and the bandwidth was 32 MHz, corresponding to an H I redshift range of $0.345 < z < 0.387$. The observations were made using the

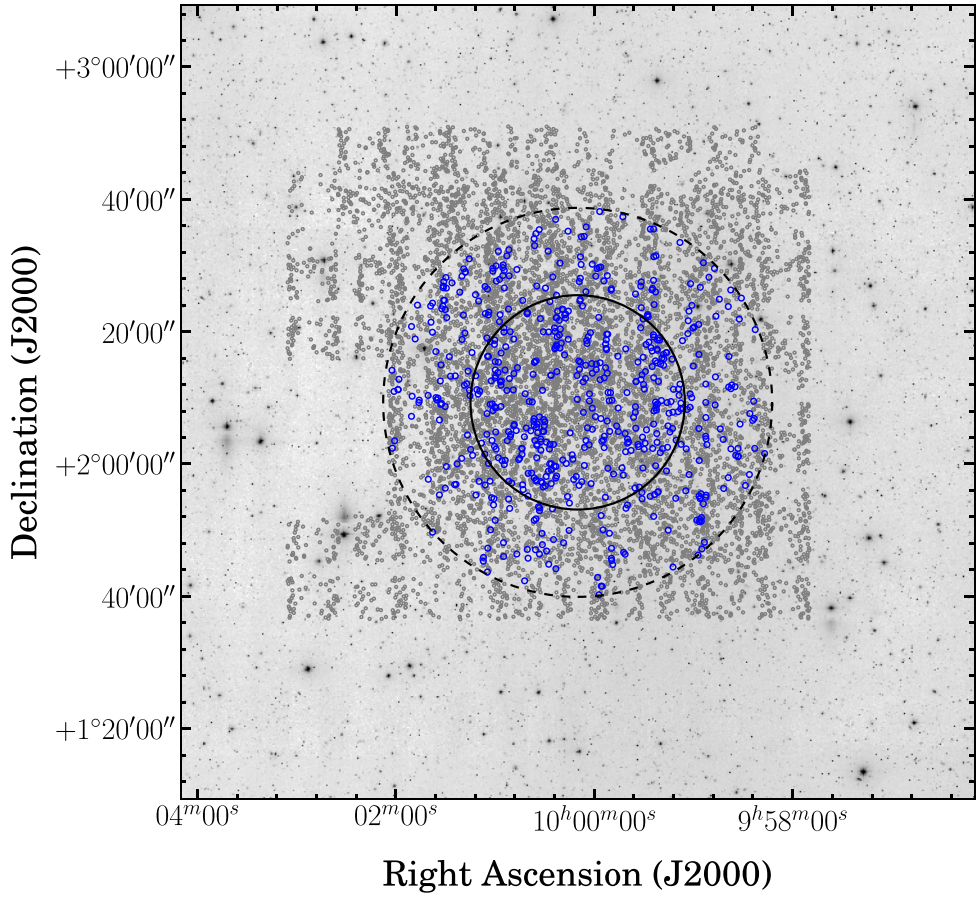

Figure 5. The spatial distribution of objects in the zCOSMOS catalogue. The blue circles denote galaxies covered by the GMRT beam and frequency. The solid and dashed circles indicate the FWHM (32.25 arcmin) and 10 per cent level (58.8 arcmin) of the GMRT primary beam at 1040 MHz, respectively.

old hardware correlator, which divided the 32-MHz bandwidth into two 16-MHz-wide sidebands. Each sideband had two polarizations and 128 spectral channels, giving a channel width of 0.125 MHz (∼36.3 km s^{-1} at $z = 0.37$). The pointing centre of the GMRT observations was RA 10$^{\rm h}$00$^{\rm m}$10$^{\rm s}$.01, Dec. +02$^{\rm d}$19$^{\rm m}$19$^{\rm s}$.95 (J2000). The primary beam size (FWHM) of the GMRT is approximately 32.25 arcmin at 1040 MHz and the 10 per cent beam level is 58.8 arcmin, which was the limit used for selecting galaxies for the stacking analysis. Observations of 3C 48, 3C 147 and 3C 286 were used to calibrate the flux density scale (Fig. 5). 0943–083 served as a phase calibrator.

3.2 Data reduction

The GMRT data reduction of the COSMOS field followed a standard reduction procedure including flagging, calibration and imaging. The GMRT data were first processed using FLAGCAL (Prasad & Chengalur 2012; Chengalur 2013), an automated flagging and calibration software developed for the GMRT data. As seen in Fig. 6, the frequency range of the COSMOS field covered by the GMRT was affected by radio frequency interference (RFI); there were also several instrumental malfunctions during the observations that caused several antennas to be unusable. The edges of each sideband were completely flagged, which led to the peak around 1040 MHz in Fig. 6, where 100 per cent of the data have been flagged. Data near 1030 MHz appear to be severely contaminated by RFI. It is known that aircraft often generate RFI at this frequency. In addition, the

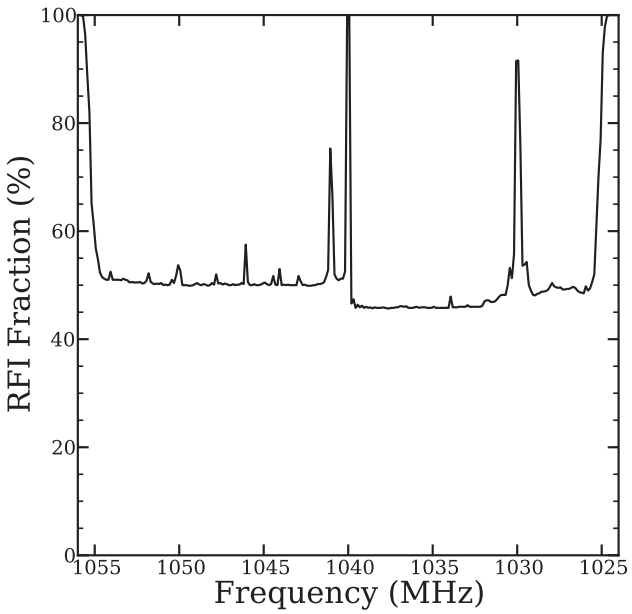

Figure 6. The fraction of flagged data after all data-reduction procedures.

GMRT front-end system had a limited dynamic range during the time when these observations were carried out, which can generate intermodulation products from strong RFI bursts. This system has since been improved significantly. About half the data in each

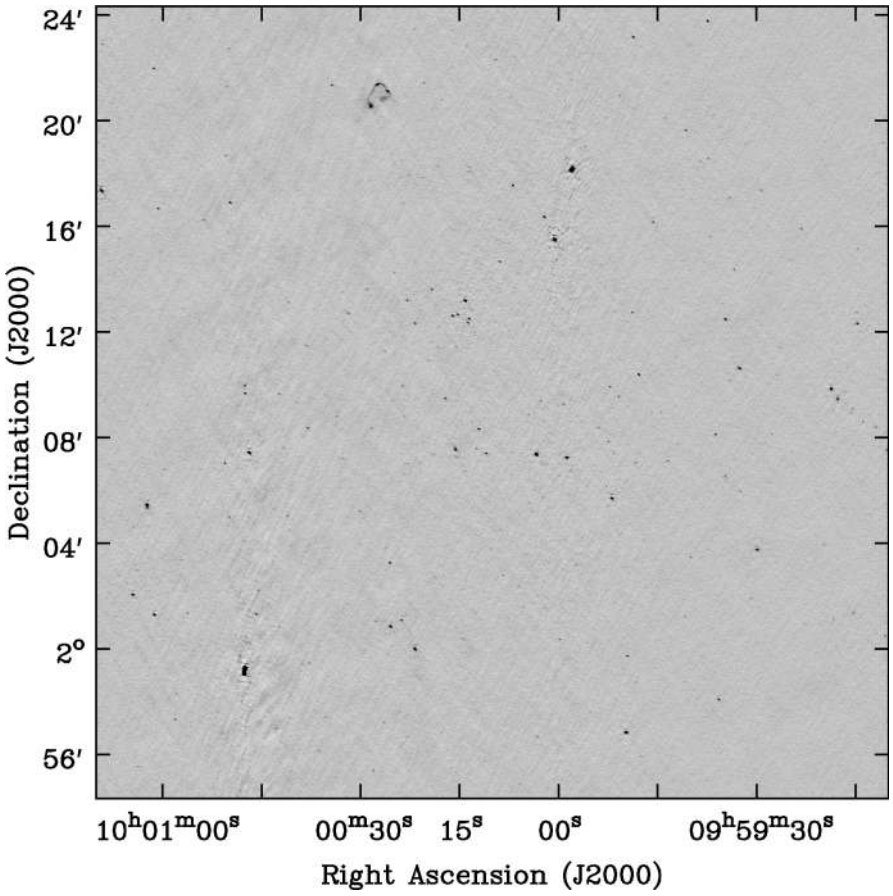

Figure 7. The central 30-arcmin area of the entire GMRT continuum image of the COSMOS field.

sideband have been flagged during iterations through the data reduction process.

Subsequent processing was done using the Common Astronomy Software Applications (CASA)[3] package (McMullin et al. 2007). If necessary, additional flagging was carried out manually, using CASA plotting and editing tools. Broad-band flux and phase calibration was done using the central 80 channels and the bandpass was determined using scans of both the flux and phase calibrators. After the calibration solutions were determined and applied, the COSMOS field data sets for each day were split and re-inspected separately as continuum images to check whether there remained any bad data appearing as artefacts in the images. Data for the 20 observing runs were then concatenated separately for each sideband. By design (Scoville et al. 2007), the COSMOS field does not contain any bright radio sources. We found that self-calibration did not improve the quality of the images significantly and hence the final analysis was performed using images without any self-calibration.

3.3 Continuum image

To make the final continuum image of the COSMOS field at $z \sim 0.37$, the central 100 channels from each sideband (lower and upper sideband) were selected and concatenated. In order to avoid bandwidth smearing, each sideband used 100 channels subdivided into 10 channel averages during the imaging. A $\sim 1 \times 1$ deg^2 continuum image was made with pixel size 0.9 arcsec pixel^{-1}, 'robust' weighting (Briggs 1995) with a robust value of 0 and the w-projection (Cornwell, Golap & Bhatnagar 2008) algorithm. The root-mean-square (rms) noise in the central regions of the final continuum (Fig. 7) is $\sim$12.3 μJy beam^{-1}, with a synthesized beam resolution of 3.5×2.4 arcsec^2. The astrometric accuracy of the GMRT imaging was determined by comparing the positions of sources detected in this image with high signal-to-noise ratio ($\geq 5\sigma$) against the positions listed in the VLA Faint Images of the Radio Sky at Twenty centimetres (FIRST) survey catalogue (Becker, White & Helfand 1995). The average positional offset found was to be $\sim$0.68 arcsec, which is less than the image pixel size of 0.9 arcsec. The maximum measured astrometric offset was 1.8 arcsec, which is still significantly smaller than the GMRT synthesized beam.

3.4 Line data cube

The spectral data cubes for the two sidebands were made with the same pixel size, robust weighting and wide-field imaging algorithm as were used to make the continuum image. The synthesized beam of the data cubes is 3.5×2.4 arcsec^2, corresponding to $\sim 17.9 \times 12.0$ kpc^2 at $z \sim 0.37$. The final spectral data cubes of each sideband were made by subtracting the continuum from these data cubes. For continuum subtraction, clean components of individual continuum sources were subtracted from the *uv* data using the CASA task '`uvsub`' and any residual continuum flux was removed in the '*image*' domain by the CASA task '`imcontsub`'. The rms noise levels per frequency channel of each sideband are $\sim$140 μJy beam^{-1}

[3] http://casa.nrao.edu

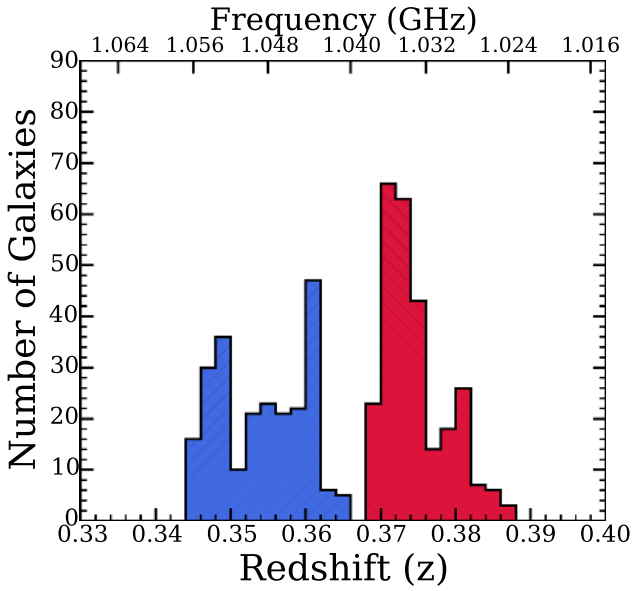

Figure 8. The redshift distribution of the COSMOS sample observed by the GMRT. Blue and red hatched areas are galaxies that lie in the upper and lower sidebands, respectively.

(lower sideband) and ∼117 μJy beam^{-1} (upper sideband), respectively.

4 STACKED H I EMISSION AND H I MASS MEASUREMENTS

Before performing the H I stacking analysis, an automated source-finding software (DUCHAMP: Whiting 2012) was used to search for any directly detected H I emitters in the final data cubes. An eyeball inspection was also done. No significant source was found by either method.

As plotted in Fig. 8, the lower and upper sideband data cubes contain 269 and 237 sample galaxies, respectively. However, some of the galaxies lie in channels seriously affected by RFI or at the edges of the data cubes. These galaxies were excluded, leaving 474 galaxies for the H I stacking analysis. The usable 474 galaxies consist of 95 galaxies with spectrophotometric Type 1, 58 with Type 2 and 321 with Type 3 or 4. Using their known positions and redshifts, the spectra for these galaxies were extracted from the data cubes with dimensions of 1 °× 1 °× 128 channels and corrected for primary beam attenuation. The GMRT primary beam pattern was assumed to have a circular Gaussian profile, given by

$$\text{gain} = \text{e}^{-(2\sqrt{\ln 2}d/\theta)^2}, \qquad \theta = 26.2 \times \frac{1280\,\text{MHz}}{f_{\text{obs}}}, \tag{1}$$

where f_{obs} is the observing frequency, θ is the half-power beam width (HPBW) and d is the angular separation from the GMRT pointing centre, given in units of arcmin. The HPBW was taken from the measurements provided on the National Centre for Radio Astrophysics (NCRA) website.[4] After this correction, the spectra were shifted and aligned to the same rest-frame velocity. The stacked spectrum was computed from a weighted average, using the rms noise of each primary beam-corrected spectrum. Stacked spectra were computed separately for the different galaxy samples, as well as for the full 474 galaxy sample.

[4] http://www.ncra.tifr.res.in

Fig. 9 shows the H I stacked spectra for each of the subtypes of galaxy. Most of the H I gas in the COSMOS field observed by the GMRT resides in Type 3 or 4 (late spiral, irregular and starburst galaxies). As expected there is no statistically significant signal from the early-type galaxies.

To calculate the average H I mass from the co-added spectra for each subsample, the following equation (Wieringa, de Bruyn & Katgert 1992) was used:

$$\frac{M_{\text{H I}}}{\text{M}_\odot} = \frac{236}{(1+z)} \left(\frac{D_L}{\text{Mpc}}\right)^2 \left(\frac{\int S_V\,\text{d}V}{\text{mJy\,km\,s}^{-1}}\right), \tag{2}$$

where z is redshift, D_L is the luminosity distance in units of Mpc and $\int S_V\,\text{d}V$ is the integrated H I emission flux in units of mJy km s^{-1}. The redshift of 0.37 is the median redshift value of stacked galaxies for this calculation, which is also used for the luminosity distance in equation (2). In calculating the integrated H I flux from the above equation, we must specify the width of the velocity window within which all the H I emission flux is contained. This velocity window is estimated from the Tully–Fisher relation (Tully & Fisher 1977). For our late-type sample galaxies, the mean w_{20} is 278.8 km s^{-1}and the maximum is ∼571 km s^{-1}. Taking into account the redshift uncertainty of the zCOSMOS survey, ±110 km s^{-1}, a velocity width of 500 km s^{-1}was used to calculate the integrated H I flux with the stacked H I spectra.

The average H I masses for each galaxy type are listed in Table 2. The errors in the average H I masses were estimated by applying a jackknife resampling method (Efron 1982). As expected, the late-type (Types 3 and 4) galaxies have higher average H I gas content than the early-type galaxies. The $M_{\text{H I}}/L_B$ ratio of the late-type galaxies is similar to the median $M_{\text{H I}}/L_B$ of Sc- and Sd-type galaxies in the local Universe (Roberts & Haynes 1994).

The above estimate of the H I mass assumes that the sample galaxies observed in H I are unresolved by the GMRT synthesized beam. To check this assumption, the sizes of sample galaxies in H I were estimated from the relationship between optical and H I properties in Broeils & Rhee (1997). These authors provided two relationships between the H I diameter and the B-band absolute magnitude, as follows:

$$\log(D_{\text{H I}}) = (-0.1673 \pm 0.0142) \times M_B - 1.9545, \tag{3}$$

$$\log(D_{\text{eff}}) = (-0.1674 \pm 0.0152) \times M_B - 2.1689, \tag{4}$$

where $D_{\text{H I}}$ is the H I diameter (in kpc) at a surface density of 1 M$_\odot$ pc^{-2} and D_{eff} is the diameter containing 50 per cent of the H I mass. Fig. 10 shows the distribution of the estimated diameters from equations (3) and (4). The blue and red histograms indicate the distribution of D_{eff} and $D_{\text{H I}}$, respectively. As can be seen, the galaxies seem to be partially resolved in terms of D_{eff} by the GMRT synthesized beam of 3.5 arcsec, while $D_{\text{H I}}$ of most galaxies is larger than the GMRT synthesized beam. We note, however, that Broeils & Rhee (1997) warned that these local correlations might be biased, due to the fact that their selection criteria required the galaxies to have large H I mass and optical size. To see whether the GMRT beam partially resolving the large galaxies causes a significant amount of H I flux to be lost, we repeated the analysis using several larger synthesized beams. The data cubes were smoothed to four additional synthesized beam sizes: 5.9, 7.8, 9.8 and 11.7 arcsec, which are equivalent to 30, 40, 50 and 60 kpc at $z \sim 0.37$, respectively. The same stacking procedure was conducted for all smoothed data cubes with different beam sizes and then the average H I masses were calculated and compared. We found no statistically significant

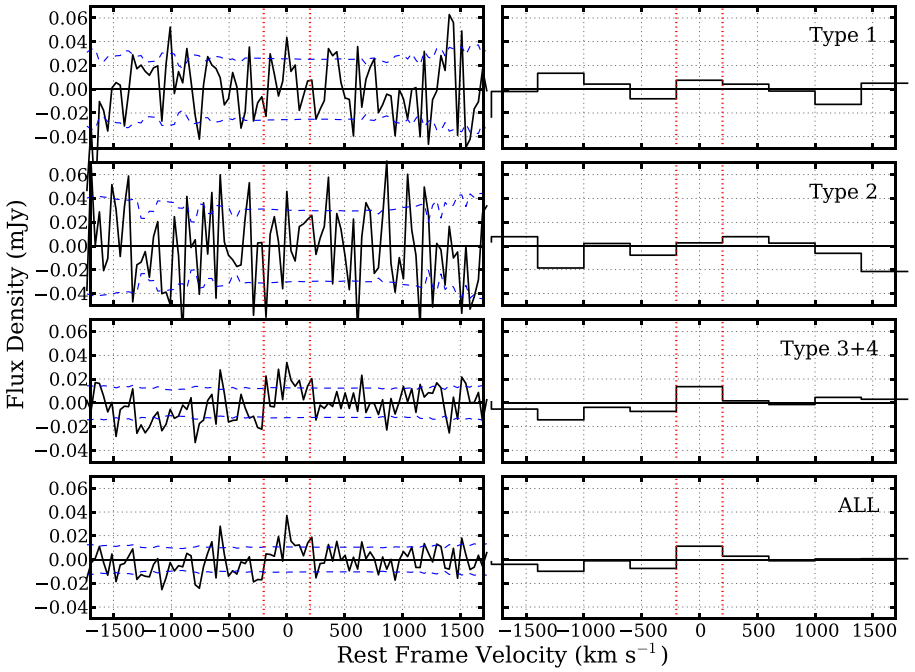

Figure 9. Stacked H I spectra of galaxies in each subgroup (left panels). The right panels show the re-binned stacked spectra with a velocity width of 500 km s^{-1}(the vertical dotted lines). The horizontal dashed line in each left panel is the 1σ error of the stacked spectrum.

Table 2. The measured properties of each galaxy type at redshift $z \sim 0.37$.

Sample	$N_{\rm gal}$	$\langle M_{\rm H\,I}\rangle$ (10^9 M$_\odot$)	$\langle L_B\rangle$ (10^9 L$_\odot$)	$\langle M_{\rm H\,I}\rangle/\langle L_B\rangle$ (M$_\odot$/L$_\odot$)	ρ_{L_B} (10^7 L$_\odot$ Mpc^{-3})	$\rho_{\rm H\,I}$ (10^7 M$_\odot$ Mpc^{-3})	f
Type 1	95	2.20 ± 2.60	17.76 ± 0.04	0.12 ± 0.15	5.11 ± 0.65	0.63 ± 0.75	–
Type 2	58	1.50 ± 2.74	21.33 ± 0.05	0.07 ± 0.13	2.69 ± 0.65	0.21 ± 0.38	1.10 ± 0.09
Type 3+4	321	3.83 ± 1.20	10.07 ± 0.01	0.38 ± 0.12	8.12 ± 2.15	4.86 ± 1.99	1.57 ± 0.02
All				$\Omega_{\rm H\,I} = (0.42 \pm 0.16) \times 10^{-3}$			

Note. $N_{\rm gal}$ is the number of galaxies that are co-added, $\langle M_{\rm H\,I}\rangle$ is the average H I mass per galaxy, $\langle L_B\rangle$ is the mean B-band luminosity, ρ_{L_B} is the luminosity density and $\rho_{\rm H\,I}$ is the H I density that the correction factor in the last column has been applied to. f is the correction factor for incomplete sampling of the luminosity function.

change in the stacked signal. For the subsequent calculations in the next sections, we hence assume that there is no significant effect of GMRT beam size on the H I stacking results.

5 COSMIC H I MASS DENSITY ($\Omega_{\rm H\,I}$)

The measured H I mass from the stacked H I spectra can be converted to an H I density ($\rho_{\rm H\,I}$) and a cosmic H I density ($\Omega_{\rm H\,I}$), allowing one to examine how the H I gas content of the Universe evolves over cosmic time. The $\Omega_{\rm H\,I}$ measurement of the COSMOS field is important because it is the highest redshift measurement ever made with an H I spectral stacking technique. While there has been a previous measurement of the H I content of galaxies at $z \sim 0.37$ (Lah et al. 2009), the sample for that study was galaxies in a rich cluster (Abell 370). Hence, unlike the current work, the results from Lah et al. (2009) cannot be used to study the evolution of the gas content of field galaxies.

In order to determine $\Omega_{\rm H\,I}$, the first step is to derive the H I density from the average H I mass ($M_{\rm H\,I}$) measured above. Simply dividing $M_{\rm H\,I}$ by the survey volume does not take into account the incompleteness of our sample to be stacked or the effect of cosmic variance. Following Rhee et al. (2013) and Delhaize et al. (2013), we made use of a volume normalization method and a correction factor to account for these effects. This approach to derive $\rho_{\rm H\,I}$ adopts the optical luminosity (L) as a weight. We determined the ratio of $M_{\rm H\,I}$ to L, which we then multiplied by the optical luminosity density (e.g. see Fall & Pei 1993). This assumes that all of the H I gas is located in galaxies with optical counterparts (Briggs 1990; Fall & Pei 1993; Rao & Briggs 1993). Several studies show that this is a reasonable assumption in the local Universe. First, the agreement between $\Omega_{\rm H\,I}$ measurements based on optically selected galaxies and those based on H I-selected samples shows that there is little neutral hydrogen gas associated with galaxies that are faint or have no optical counterparts (Fall & Pei 1993; Rao & Briggs 1993; Zwaan et al. 1997). Furthermore, large blind 21-cm surveys have found that optically invisible but gas-rich galaxies below optical detection threshold do not exist in numbers sufficiently large to bias the inventory of $\rho_{\rm H\,I}$ (Doyle et al. 2005; Taylor & Webster 2005).

Accurate photometric measurements of luminosity, which are needed to normalize the stacked H I measurement, are available for the COSMOS field, as discussed in Section 2.2. Thanks to a wealth of photometric and spectroscopic data available, the luminosity functions and luminosity densities have been quite well measured up to $z \sim 1$ in the COSMOS field (Zucca et al. 2009). Since our

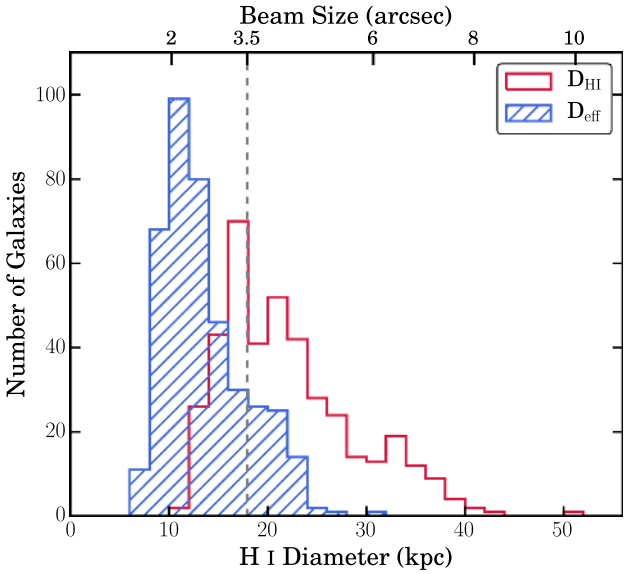

Figure 10. H I size distribution of the zCOSMOS sample derived using the relation between optical magnitude and H I size based on Broeils & Rhee (1997). Two H I sizes defined differently are used. Blue (/) and red histograms denote effective H I diameter and H I diameter at a surface density of 1 $M_\odot$ pc^{-2}, respectively. The GMRT synthesized beam size is shown as a vertical dashed line.

galaxy classification scheme is the same as that used in Zucca et al. (2009), the luminosity function and luminosity density derived in that article can be adopted directly to derive $\rho_{\rm H\,I}$. The equations below are used to derive H I density for each galaxy type:

$$\sum M_{\rm H\,I} = \langle M_{\rm H\,I}\rangle \times N_{\rm gal}, \quad \rho_{\rm H\,I} = \frac{\sum M_{\rm H\,I}}{\sum L_B} \times \rho_{L_B}(z), \tag{5}$$

where $\langle M_{\rm H\,I}\rangle$ denotes the average H I mass measured using the H I stacking technique, $N_{\rm gal}$ is the number of co-added galaxies and L_B and ρ_{L_B} are luminosity and luminosity density of the zCOSMOS sample galaxies in the B band, respectively. We calculated the H I gas density separately for each galaxy type from Type 1, Type 2 and Type 3+4. However, this H I density is calculated without accounting for galaxies fainter than the optical survey limit. In the nearby Universe, the low-luminosity late-types are known to be gas-rich, so we need to make a first-order compensation for the fact that these objects are not all represented in our sample. To correct for this incomplete sampling of the luminosity function, correction factors for each type were obtained using the luminosity function parameters such as the faint-end slope (α) and characteristic luminosity (L^*) of the luminosity function given by Zucca et al. (2009). We refer the reader to Appendix A in Rhee et al. (2013) for more details about the correction-factor calculation. This correction factor was not applied to early-type galaxies, because the contribution of the faint early-type population to $M_{\rm H\,I}$ and $\rho_{\rm H\,I}$ is small. Moreover, the correction factor for the early-type sample (Type 1) made no difference in the calculation of the total $\rho_{\rm H\,I}$. These correction factors, as well as the corrected $\rho_{\rm H\,I}$ for each type, are listed in Table 2.

Consistent with earlier works, we define the cosmic H I gas density ($\Omega_{\rm H\,I}$) as the ratio of $\rho_{\rm H\,I}$ to the critical density ($\rho_{\rm crit}$):

$$\Omega_{\rm H\,I} = \frac{\rho_{\rm H\,I}}{\rho_{\rm crit}} = \frac{8\pi G \rho_{\rm H\,I}}{3H_0^2}, \tag{6}$$

where H_0 is the Hubble constant and G is the gravitational constant. The critical density at present is $\rho_{\rm crit} = 2.78 \times 10^{11} h^2$ $M_\odot$ Mpc^{-3}, where $h = H_0/100$ km s^{-1} ($h = 0.7$). Since, in principle, all galaxy types contribute to the cosmic H I density, the total $\rho_{\rm H\,I}$ is obtained by summing $\rho_{\rm H\,I}$ contributions from all types. This gives $\Omega_{\rm H\,I} = (0.42 \pm 0.16) \times 10^{-3}$. This 2.6$\sigma$ measurement is shown in Fig. 11, along with other available measurements taken from the literature (see the caption for more details). As can be seen, our measurement, taken in conjunction with earlier measurements at lower redshifts, indicates that there has been no significant evolution in $\Omega_{\rm H\,I}$ from $z = 0$ to $z \sim 0.4$. The weighted mean average of $\Omega_{\rm H\,I}$ from all 21-cm measurements at redshifts $z < 0.4$ gives $\Omega_{\rm H\,I} = (0.35 \pm 0.01) \times 10^{-3}$.

Regarding the cosmic variance, it is known that the zCOSMOS field suffers less than 10 per cent cosmic variance in the redshift interval $z = 0$–0.5 (Driver & Robotham 2010). The zCOSMOS field surveyed for this article by the GMRT has a limited redshift interval of $0.345 < z < 0.387$ and a small sky area compared with the original, which would result in increased cosmic variance. However, since in our $\Omega_{\rm H\,I}$ calculation above we perform a volume normalization using luminosity density derived from the full sample of the zCOSMOS field, the cosmic variance that we are subject to is the same as that computed for the entire zCOSMOS field. Moreover, we compared the luminosity density of the zCOSMOS field at $z \sim 0.37$ used for volume normalization with that derived from a large and complete spectroscopic survey, such as Galaxy and Mass Assembly (GAMA: Loveday et al. 2012). The two luminosity densities are in excellent agreement for the overall galaxy population, as well as for each galaxy population. This implies that the volume we used for normalization can represent the average of the Universe at the redshift we explored.

The stacking analysis using 21-cm emission carried out in this article is based on the assumption that H I gas in our galaxies is optically thin. This means that any possible influence of H I self-absorption, which will lead to an underestimation of the H I mass, is negligible. Since it is very difficult to assess the effect quantitatively and statistically, even large blind H I surveys have made only a rough estimate for the effect, i.e. an underestimation of less than 15 per cent in $\Omega_{\rm H\,I}$ (Zwaan et al. 1997, 2005). However, based on high-resolution maps of the H I distribution in M31, M32 and the Large Magellanic Cloud, Braun (2012) recently suggested that galaxies contain a significant population of H I clouds with a size of 100 pc and high H I column density ($>10^{23}$ cm^{-2}), which are optically thick. He derived a global opacity correction factor of 1.34 ± 0.05 and applied this to the local $\Omega_{\rm H\,I}$ measurements, resulting in ∼34 per cent increased $\Omega_{\rm H\,I}$, as seen in Fig. 11. Although the sample used to derive the correction factor covers a fairly large range of H I mass, the total number of galaxies in his sample is very small. As such, the validity of applying this correction factor to high-redshift measurements like ours seems to be unclear. In any case, were this correction to be uniformly applied to all H I emission surveys, it would result only in a shift of all the values upwards and would not affect the conclusion that there appears to be no evolutionary trend in $\Omega_{\rm H\,I}$, at least out to $z \lesssim 0.4$.

6 H I GAS EVOLUTION OVER LAST 4 GYR

In Fig. 11, our $\Omega_{\rm H\,I}$ measurement of the COSMOS field is compared with other $\Omega_{\rm H\,I}$ values available in the published literature (Prochaska et al. 2005; Zwaan et al. 2005; Rao et al. 2006; Lah et al. 2007; Noterdaeme et al. 2009, 2012; Martin et al. 2010; Freudling et al. 2011; Delhaize et al. 2013; Rhee et al. 2013, 2016; Zafar et al.

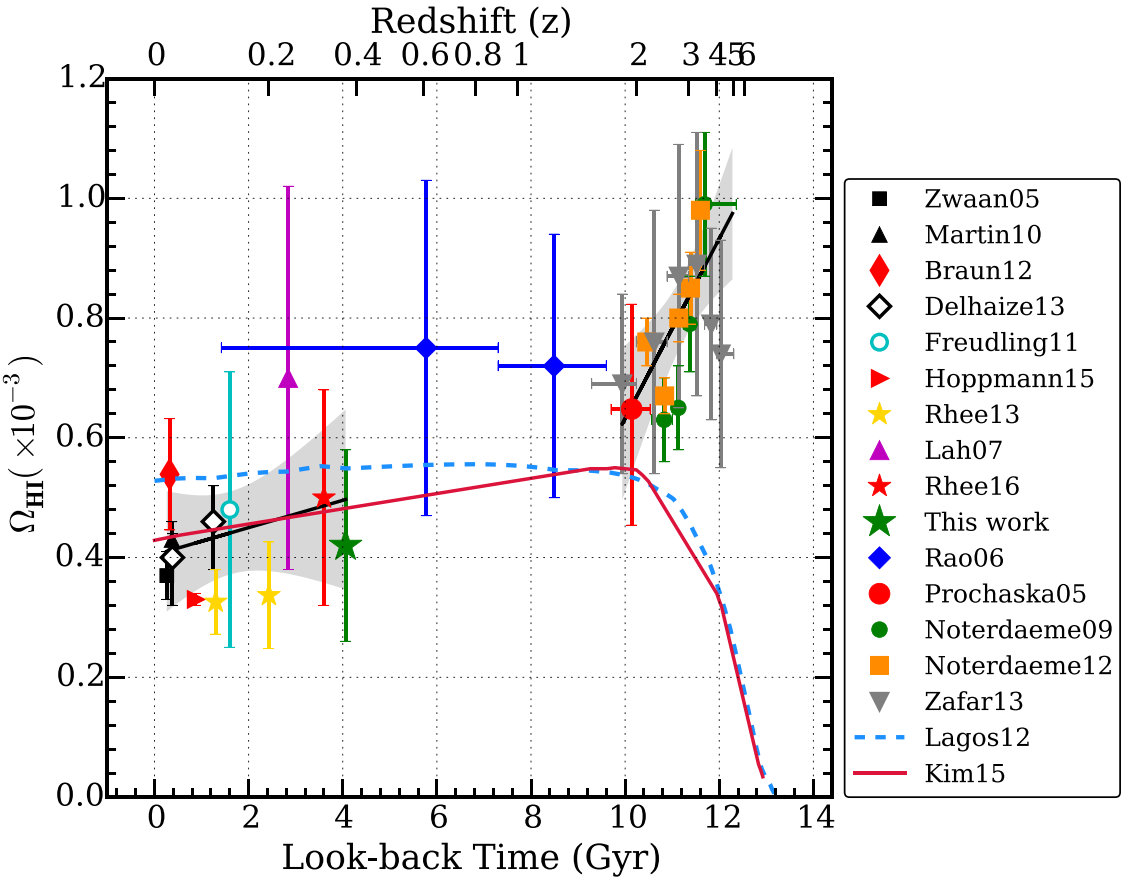

Figure 11. The cosmic H I gas density ($\Omega_{\rm H\,I}$) measurements as a function of redshift (top axis) and look-back time (bottom axis). All measurements have been corrected to the same cosmological parameters. Our $\Omega_{\rm H\,I}$ measurement of the COSMOS field is presented by the green star. The small black square and triangle at $z \sim 0$ are the HIPASS and ALFALFA 21-cm emission measurements by Zwaan et al. (2005) and Martin et al. (2010), respectively. The red diamond is not a measured value but the average $\Omega_{\rm H\,I}$ of the two measurements at $z = 0$, to which a correction factor for the self-opaque effect has been applied (Braun 2012). The open diamonds are from the Parkes telescope and an H I stacking technique (Delhaize et al. 2013). The cyan open circle is the preliminary result from the Arecibo Ultra Deep Survey (AUDS) (Freudling et al. 2011). The red right-pointing triangle is the 21-cm direct detection measurement from 60 per cent data of the total AUDS survey (Hoppmann et al. 2015). Two yellow stars are measured by Rhee et al. (2013) using the WSRT and stacking technique. The big purple triangle is measured by Lah et al. (2007) using the GMRT 21-cm emission stacking. The red star is the $\Omega_{\rm H\,I}$ measurement of the VIMOS VLT Deep Survey (VVDS) 14 h field at $z \sim 0.32$ (Rhee et al. 2016, in preparation) using the GMRT along with a stacking technique. The blue diamonds, red big circle, green circles and orange squares are damped Lyman-α measurements from the *HST* and the Sloan Digital Sky Survey (SDSS) by Rao, Turnshek & Nestor (2006), Prochaska, Herbert-Fort & Wolfe (2005), Noterdaeme et al. (2009) and Noterdaeme et al. (2012), respectively. The grey downward triangles at a high redshift of $z > 2$ are ESO Ultraviolet and Visual Echelle Spectrograph (UVES) measurements of DLAs and sub-DLAs by Zafar et al. (2013). The black lines with grey shaded areas are least-squares fits and their 95 per cent confidence interval with all $\Omega_{\rm H\,I}$ measurements at lower redshifts and higher redshifts, respectively. The blue dashed and red solid lines are model predictions of $\Omega_{\rm H\,I}$ taken from Lagos et al. (2014) and Kim et al. (2015), respectively.

2013; Hoppmann et al. 2015). Two main observational techniques have been used to measure $\Omega_{\rm H\,I}$: 21-cm emission observations at low redshifts and damped Lyman alpha absorption (DLA) observations at high redshifts. All measurements using H I 21-cm emission from both direct detection and stacking are in good agreement. At high redshifts ($z > 2$), all $\Omega_{\rm H\,I}$ measurements from DLA observations are consistent with one another, showing an increase in $\Omega_{\rm H\,I}$ with redshift. Also there seems to be at least two times more H I gas than at lower redshifts. We note that the H I 21-cm measurements correspond to the H I gas inside galaxies, while the DLA observations measure the total gas, regardless of whether it lies inside or outside galaxies. In principle these could be different quantities, although, as noted above, in the local Universe at least, there is no evidence for a large reservoir of H I that lies in optically dark galaxies.

Many galaxy evolution models have recently attempted to predict H I gas densities across cosmic time to reproduce observations (e.g. Power, Baugh & Lacey 2010; Lagos et al. 2011, 2014; Duffy et al. 2012; Davé et al. 2013; Kim et al. 2015; Rahmati et al. 2015). However, there is a tension between observations and theoretical models. In Fig. 11, we show theoretical predictions for the evolution of $\Omega_{\rm H\,I}$ from the recent semi-analytic 'Lagos12' and 'Kim15' models of Lagos et al. (2014) and Kim et al. (2015) for comparison between observations and theories. As can be seen, the theoretical models do match the low-redshift data, but not the high-redshift DLA based measurements. In contrast, a hydrodynamical simulation study of the distribution of H I around high-redshift galaxies at $z > 1$ (e.g. Rahmati et al. 2015) shows that their $\Omega_{\rm H\,I}$ predictions are in good agreement with the $\Omega_{\rm H\,I}$ evolution at high redshifts, while they disagree with the lower redshift $\Omega_{\rm H\,I}$. In some simulations, this problem is interpreted as reflecting the difference between what the H I 21-cm measurements and the DLA measurements are sensitive to (Altay et al. 2011; Faucher-Giguère & Kereš 2011; Fumagalli et al. 2011). The forthcoming surveys by the SKA pathfinders and the SKA itself will be critically important to resolve this issue.

7 SUMMARY AND CONCLUSION

We present the results of an H I spectral stacking analysis using GMRT observations of the COSMOS field. Our sample is chosen from the zCOSMOS-bright 10k catalogue (Lilly et al. 2009). The individual H I 21-cm line spectra obtained from the GMRT are stacked using the known optical positions and redshifts of the galaxies. The H I spectra are stacked separately for galaxy types classified by SED template-fitting and then converted to the average H I mass per galaxy. We find that the H I signal comes primarily from late-type galaxies, as expected. The inferred $M_{\rm H\,I}/L_B$ ratio is consistent with that of galaxies in the local ($z = 0$) Universe. Using the average H I mass, along with the integral optical B-band luminosity of the sample galaxies and the luminosity density of the COSMOS field, a volume normalization is applied to obtain the cosmic H I density ($\Omega_{\rm H\,I}$). We measure $\Omega_{\rm H\,I} = (0.42 \pm 0.16) \times 10^{-3}$ at $z \sim 0.37$. This 2.6σ measurement is the highest redshift measurement of $\Omega_{\rm H\,I}$ ever made using H I spectral stacking. The value of $\Omega_{\rm H\,I}$ that we measure is consistent, within the error bars, with both the $\Omega_{\rm H\,I}$ at $z = 0$ as measured from large blind 21-cm surveys and that measured from other H I stacking experiments. All the H I 21-cm emission measurements to date show no evidence for evolution of H I gas abundance over the last 4 Gyr; the weighted mean of $\Omega_{\rm H\,I}$ from all 21-cm measurements at $z < 0.4$ is $(0.35 \pm 0.01) \times 10^{-3}$. This value of $\Omega_{\rm H\,I}$ is, however, smaller than that measured at $z \gtrsim 2$ from DLA observations. The next generation of radio telescopes will be sensitive enough to detect the H I signal to redshifts greater than $z = 1$ and will be crucial in understanding the evolution of $\Omega_{\rm H\,I}$ in the redshift range intermediate between $z \sim 0.4$ and the redshifts probed by DLA observations.

ACKNOWLEDGEMENTS

We are grateful to an anonymous referee for helpful comments and suggestions that improved this work. JR thanks Lister Staveley-Smith for useful comments. We thank Claudia del P. Lagos and Han-Seek Kim for providing their model predictions used in Fig. 11. We also thank the staff of the GMRT for their assistance. The GMRT is operated by the National Centre for Radio Astrophysics of the Tata Institute of Fundamental Research. This research was funded by an Australian Indian Strategic Research Fund (AISRF) grant. This fund was jointly administered by the Department of Innovation, Industry, Science and Research in Australia and by the Department of Science and Technology in India. The project title was 'Gas in Galaxies in the Distant Past'. Parts of this research were conducted by the Australian Research Council Centre of Excellence for All-sky Astrophysics (CAASTRO), through project number CE110001020. The G10/COSMOS cutout tool uses data acquired as part of the Cosmic Evolution Survey (COSMOS) project and spectra from observations made with ESO Telescopes at the La Silla or Paranal Observatories under programme ID 175.A-0839. The G10/COSMOS cutout tool is hosted and maintained by funding from the International Centre for Radio Astronomy Research (ICRAR) at the University of Western Australia. Full details of the catalogue can be found in (Davies et al. 2015) or on the G10 website at http://ict.icrar.org/cutout/G10/.

REFERENCES

Altay G., Theuns T., Schaye J., Crighton N. H. M., Dalla Vecchia C., 2011, ApJ, 737, L37
Arnouts S., Cristiani S., Moscardini L., Matarrese S., Lucchin F., Fontana A., Giallongo E., 1999, MNRAS, 310, 540
Becker R. H., White R. L., Helfand D. J., 1995, ApJ, 450, 559
Bertoldi F. et al., 2007, ApJS, 172, 132
Blyth S. et al., 2015, Advancing Astrophysics with the Square Kilometre Array (AASKA14). SISSA, Trieste, PoS#128
Braun R., 2012, ApJ, 749, 87
Briggs F. H., 1990, AJ, 100, 999
Briggs D. S., 1995, PhD thesis, New Mexico Institute of Mining and Technology
Broeils A. H., Rhee M.-H., 1997, A&A, 324, 877
Capak P. et al., 2007, ApJS, 172, 99
Cassata P. et al., 2007, ApJS, 172, 270
Chengalur J. N., 2013, NCRA Techincal Report, NCRA/COM/001. National Centre for Radio Astrophysics, India
Chengalur J. N., Braun R., Wieringa M., 2001, A&A, 372, 768
Colless M. et al., 2001, MNRAS, 328, 1039
Cornwell T. J., Golap K., Bhatnagar S., 2008, IEEE Journal of Selected Topics in Signal Processing, 2, 647
Davé R., Katz N., Oppenheimer B. D., Kollmeier J. A., Weinberg D. H., 2013, MNRAS, 434, 2645
Davies L. J. M. et al., 2015, MNRAS, 447, 1014
Delhaize J., Meyer M. J., Staveley-Smith L., Boyle B. J., 2013, MNRAS, 433, 1398
Doyle M. T. et al., 2005, MNRAS, 361, 34
Driver S. P., Robotham A. S. G., 2010, MNRAS, 407, 2131
Duffy A. R., Kay S. T., Battye R. A., Booth C. M., Dalla Vecchia C., Schaye J., 2012, MNRAS, 420, 2799
Efron B., 1982, The Jackknife, the Bootstrap and other resampling plans, CBMS-NSF Regional Conference Series in Applied Mathematics. Society for Industrial and Applied Mathematics (SIAM), Philadelphia
Fall S. M., Pei Y. C., 1993, ApJ, 402, 479
Faucher-Giguère C.-A., Kereš D., 2011, MNRAS, 412, L118
Fernández X. et al., 2013, ApJ, 770, L29
Freudling W. et al., 2011, ApJ, 727, 40
Fumagalli M., Prochaska J. X., Kasen D., Dekel A., Ceverino D., Primack J. R., 2011, MNRAS, 418, 1796
Hasinger G. et al., 2007, ApJS, 172, 29
Haynes M. P. et al., 2011, AJ, 142, 170
Holwerda B. W., Blyth S.-L., Baker A. J., 2012, in Tuffs R. J., Popescu C. C., eds, Proc. IAU Symp. 284, The Spectral Energy Distribution of Galaxies. Cambridge Univ. Press, Cambridge, p. 496
Hoppmann L., Staveley-Smith L., Freudling W., Zwaan M. A., Minchin R. F., Calabretta M. R., 2015, MNRAS, 452, 3726
Ilbert O. et al., 2006, A&A, 457, 841
Ilbert O. et al., 2009, ApJ, 690, 1236
Kim H.-S., Wyithe J. S. B., Power C., Park J., Lagos C. d. P., Baugh C. M., 2015, MNRAS, 453, 2315
Koekemoer A. M. et al., 2007, ApJS, 172, 196
Koribalski B. S., Staveley-Smith L., 2009, ASKAP Survey Science Proposal: WALLBY
Lagos C. D. P., Baugh C. M., Lacey C. G., Benson A. J., Kim H.-S., Power C., 2011, MNRAS, 418, 1649
Lagos C. D. P., Baugh C. M., Zwaan M. A., Lacey C. G., Gonzalez-Perez V., Power C., Swinbank A. M., van Kampen E., 2014, MNRAS, 440, 920
Lah P. et al., 2007, MNRAS, 376, 1357
Lah P. et al., 2009, MNRAS, 399, 1447
Lilly S. J. et al., 2007, ApJS, 172, 70
Lilly S. J. et al., 2009, ApJS, 184, 218
Loveday J. et al., 2012, MNRAS, 420, 1239
Martin D. C. et al., 2005, ApJ, 619, L1
Martin A. M., Papastergis E., Giovanelli R., Haynes M. P., Springob C. M., Stierwalt S., 2010, ApJ, 723, 1359
Meyer M. J., 2009, in Heald G., Serra P., eds, Proc. Panoramic Radio Astronomy: Wide-field 1–2 GHz research on galaxy evolution
Meyer M. J. et al., 2004, MNRAS, 350, 1195
Meyer M., Robotham A., Obreschkow D., Driver S., Staveley-Smith L., Zwaan M., 2015, Advancing Astrophysics with the Square Kilometre Array (AASKA14). SISSA, Trieste, PoS#131

McMullin J. P., Waters B., Schiebel D., Young W., Golap K., 2007, in Shaw R. A., Hill F., Bell D. J., eds, ASP Conf. Ser. Vol. 376, Astronomical Data Analysis Software and Systems XVI. Astron. Soc. Pac., San Francisco, CA, p. 6
Noterdaeme P., Petitjean P., Ledoux C., Srianand R., 2009, A&A, 505, 1087
Noterdaeme P. et al., 2012, A&A, 547, L1
Power C., Baugh C. M., Lacey C. G., 2010, MNRAS, 406, 43
Prasad J., Chengalur J., 2012, Experimental Astronomy, 33, 157
Prochaska J. X., Herbert-Fort S., Wolfe A. M., 2005, ApJ, 635, 123
Rahmati A., Schaye J., Bower R. G., Crain R. A., Furlong M., Schaller M., Theuns T., 2015, MNRAS, 452, 2034
Rao S., Briggs F., 1993, ApJ, 419, 515
Rao S. M., Turnshek D. A., Nestor D. B., 2006, ApJ, 636, 610
Rhee J., Zwaan M. A., Briggs F. H., Chengalur J. N., Lah P., Oosterloo T., Hulst T. V. D., 2013, MNRAS, 435, 2693
Roberts M. S., Haynes M. P., 1994, ARA&A, 32, 115
Sanders D. B. et al., 2007, ApJS, 172, 86
Santos M., Alonso D., Bull P., Silva M. B., Yahya S., 2015, in Bourke T. L. et al., eds, Advancing Astrophysics with the Square Kilometre Array (AASKA14). SISSA, Trieste, PoS#019
Schinnerer E. et al., 2004, AJ, 128, 1974
Schinnerer E. et al., 2007, ApJS, 172, 46
Schlegel D. J., Finkbeiner D. P., Davis M., 1998, ApJ, 500, 525
Scoville N. et al., 2007, ApJS, 172, 1
Skrutskie M. F. et al., 2006, AJ, 131, 1163
Staveley-Smith L., Oosterloo T., 2015, in Bourke T. L. et al., eds, Advancing Astrophysics with the Square Kilometre Array (AASKA14). SISSA, Trieste, PoS#167
Taniguchi Y. et al., 2007, ApJS, 172, 9
Tasca L. A. M. et al., 2009, A&A, 503, 379
Taylor E. N., Webster R. L., 2005, ApJ, 634, 1067
Tully R. B., Fisher J. R., 1977, A&A, 54, 661
Whiting M. T., 2012, MNRAS, 421, 3242
Wieringa M. H., de Bruyn A. G., Katgert P., 1992, A&A, 256, 331
Williams R. J., Quadri R. F., Franx M., van Dokkum P., Labbé I., 2009, ApJ, 691, 1879
York D. G. et al., 2000, AJ, 120, 1579
Zafar T., Péroux C., Popping A., Milliard B., Deharveng J.-M., Frank S., 2013, A&A, 556, A141
Zamojski M. A. et al., 2007, ApJS, 172, 468
Zucca E. et al., 2009, A&A, 508, 1217
Zwaan M. A., Briggs F. H., Sprayberry D., Sorar E., 1997, ApJ, 490, 173
Zwaan M. A., van Dokkum P. G., Verheijen M. A. W., 2001, Sci, 293, 1800
Zwaan M. A., Meyer M. J., Staveley-Smith L., Webster R. L., 2005, MNRAS, 359, L30

This paper has been typeset from a TEX/LATEX file prepared by the author.